

SWIR albedo mapping of Mars using Mars Orbiter Mission data

Ramdayal Singh^{1,2}, Manoj K. Mishra¹ and Prakash Chauhan^{1,*}

¹Space Applications Centre, Indian Space Research Organisation, Ahmedabad 380 005, India

²Faculty of Science, NIRMA University, Ahmedabad 382 481, India

Global apparent short wave infrared (SWIR) (1.64–1.66 μm) albedo mapping results from data acquired by Methane Sensor for Mars (MSM) onboard Indian Mars Orbiter Mission from October 2014 to February 2015, are presented. Global analysis of low and high albedo patterns is discussed using MSM apparent SWIR albedo map. The occurrence frequency of MSM apparent SWIR albedo shows a clear bimodal behaviour and is in good agreement with OMEGA NIR albedo distribution. Based on MSM apparent SWIR albedo values, three classes (high, intermediate and low albedo values) are defined, which show a clear elevation dependency. Variation of weekly average apparent albedo during the study period over Syrtis Major, Daedalia Planum and Valles Marineris region, respectively, is presented.

Keywords: Albedo, Mars, methane sensor for Mars.

THE Martian surface albedo mapping has remained an object of interest for the Earth-based astronomers for centuries. A number of surface markings of Mars have been produced using improved telescopic observation, which enable observers to assign relative quantitative albedo to major features. However absolute calibration of albedo was not possible^{1,2}. In the last three to four decades the Martian surface albedo mapping has considerably improved when spacecrafts carried the high-resolution imaging systems to the Mars. The magnitudes and spatial distributions of Martian surface albedo are important inputs for a variety of interdisciplinary studies of Mars. Surface albedo, i.e. the fraction of solar incident light reflected into the atmosphere from the Martian surface acts as a driving force for meteorological systems, thus providing important boundary conditions for global circulation model (GCM) calculations. The meteorological conditions in turn place constraints on present and future spacecraft and mission designs. Various Mars missions have provided the albedo maps of Mars at different wavelength ranges, e.g. Infrared thermal mapper IRTM (20 μm) albedo map from Viking mission^{3,4}; infrared imaging spectrometer (ISM) albedo map from Phobos^{5,6}; 1 μm Martian surface reflectivity map from spectroscopic observations in 0.3 μm to 50 μm (ref. 7); Hubble Space

Telescope (HST) Mars' reflectivity at 1.042 μm (ref. 8); Mars Global Surveyor Thermal Emission Spectrometer (TES) derived albedo map⁹; Mars Orbiter Laser Altimeter (MOLA) derived reflectivity of Mars using active sounding¹⁰; and The Observatoire pour la Minéralogie, l'Eau, les Glaces et l'Activité OMEGA near-infrared (NIR) (1.08 μm) derived albedo¹¹, MOLA derived reflectivity of Mars using passive radiometry¹² and MOLA derived reflectivity of Mars using active and passive radiometry¹³. All of the albedo maps derived from different Mars missions at different times show variations in albedo due to variability in the atmosphere of Mars associated with the seasonal transport of dust.

In the present paper we have presented the global apparent short wave infra-red (SWIR) (1.65 μm) albedo map derived from data acquired by Methane Sensor for Mars (MSM) onboard Indian Mars Obiter Mission (MOM) from October 2014 to February 2015. Based on correlation of global MSM apparent SWIR albedo with elevations, the Martian surface has been classified into three classes (high, intermediate and low albedo regions) and the occurrence frequency of these classes with respect to elevation is discussed. Comparative analysis of low and high albedo patterns is discussed using MSM SWIR and OMEGA NIR derived albedo maps. Apparent albedo variation with respect to solar longitude is represented over Syrtis Major, Daedalia Planum and Valles Marineris regions, respectively.

Methane Sensor for Mars (MSM) that has been developed at Space Applications Centre of the Indian Space Research Organisation (ISRO) aims to measure methane in Martian atmosphere with parts per billion (ppb) accuracy and map its resources. The mission has a highly elliptical orbit of 372 \times 80,000 km that facilitates both localized observations with higher spatial resolution as well as observations with large coverage and high radiometric and temporal resolutions. The instrument is designed as a differential radiometer in SWIR region of the electromagnetic spectrum with a spectral range of 1.64 to 1.66 μm (ref. 14). MSM measures reflected solar radiance in two SWIR (1.64 to 1.66 μm) channels. There is absorption by CH₄ in the first channel (methane channel) and no absorption in the second spectral channel (reference channel). The salient features of MSM are tabulated in Table 1.

Table 1. Salient features of methane sensor for Mars

Parameter	Value
Resolution (km)	0.63 at Periareion and 135 at Apoareion
Swath (km)	4.4 at Periareion and 948 at Apoareion
Spectral region	1.64 μm to 1.66 μm
Integration time (ms)	0.25, 0.5, 1 and 2 (selectable)
Quantization (bits)	20 (internally binned)
Data rate (Mbps)	2.1875

*For correspondence. (e-mail: prakash@sac.isro.gov.in)

Reference channel radiance data acquired by MSM from October 2014 to February 2015 was used for apparent SWIR albedo mapping. For each pixel the values for phase, solar incidence and emission angles were available. Since spatial resolution of the observations depends on the orbit condition, the MSM data acquired on different dates has different spatial resolution. Before using MSM datasets, a number of constraints depending on sun-sensor geometry were applied for filtration of data as described in the next paragraph. All MSM datasets were provided with calibration files having gain and bias factors for 8 pixels of methane channel and 8 pixels of reference channel. Calibration files for different integration time were provided separately. Appropriate calibration files were used for converting MSM reference channel count number to radiance value. Along with MSM data, the elevation data obtained from MOLA digital elevation model¹⁰ and OMEGA NIR albedo map¹⁵ have also been used in the present study for analysis.

The albedo of the surface is defined as the fraction of incident solar radiation reflected (and hence not absorbed) by the surface. However, in this case, since no atmospheric correction was made, the albedo will be the combined reflectivity due to surface as well as atmosphere, which is known as apparent albedo. Few restrictions were placed on the data before the albedo map preparation. Data less than 1° of the limb of the planet was discarded, to be certain that the field of view was entirely on the planet and also to avoid atmospheric limb brightening. Data with incidence and solar zenith angle greater than 60° was also discarded to minimize the atmospheric effects.

The MSM SWIR (1.64 μm –1.66 μm) channel radiance data was converted to top of atmosphere reflectance (I/F) using the observation constraints and a solar spectrum scale to Mars–Sun distance. The I/F is defined as $I/F = \pi L / (F_0 \cos(i) \cos(\theta_0))$, where L , i and θ_0 refer to the SWIR channel radiance observed by MSM, the incidence angle and the solar zenith angle, respectively. F_0 is the Mars–Sun distance corrected top of the atmosphere SWIR channel integrated incoming solar flux per unit of surface assuming a Lambertian surface. These I/F values are used for producing the SWIR albedo map of the Martian surface. The average value of albedo for each pixel is mapped to a grid with 180 latitude bins and 360 longitude bins, providing an effective spatial resolution of 1° latitude by 1° longitude. It is to be noted that atmosphere and dust rejection criteria were not applied on this albedo map.

Figure 1 shows the globe views of MSM derived Martian apparent SWIR albedo map. The bright regions (albedo greater than 0.4) are mainly localized over the Tharsis plateau, Arbia Terra and Elysium Planitia. Low albedo regions (<0.15) are mainly localized in Syrtis Major and Southern highlands, although low albedo regions such as Acidalia (<0.17) are also identified in the

Northern hemisphere. In general low albedo values are associated with darker surface on Mars having volcanic rock basalt as surface exposures. Higher albedo values represent surface covered by dust. The area shown in blue colour indicates the presence of basaltic composition while red indicates the dust covered regions of Mars. The general appearance of the map is similar to that of previous observations of albedo^{3,15,16}. The discrepancies with some of the previous observations could result from physical processes such as temporal variations of the contribution of aerosols, photometric effects due to different geometries of observations.

From Figure 1 it is clear that the MSM data coverage is mainly confined between latitudes $\pm 50^\circ$. Therefore, for comparison with OMEGA NIR albedo values¹⁵ the Martian region was restricted between $\pm 50^\circ$ latitude as shown in Figure 2 (equi-rectangular view of MSM apparent SWIR albedo map). It has been reported in Ody *et al.*¹⁵ that the OMEGA NIR albedo map used in the present study was generated by OMEGA 1 μm data acquired from January 2004 to August 2010. Figure 3 shows normalized frequency of occurrence for MSM apparent SWIR and for OMEGA NIR albedo for the region shown in Figure 2. The general pattern of frequency curve of MSM apparent SWIR albedo is similar to OMEGA NIR albedo. However, there is shifting of MSM and OMEGA albedo because of difference in wavelength channels. It is to be noted that apart from wavelength differences, calibration differences may also contribute to shifting of MSM and OMEGA albedo. The frequency of occurrence of albedos shows a bimodal distribution. Figures 3 and 4 *a* show good correlation between MSM apparent SWIR and OMEGA NIR albedos.

We define three classes of Martian region based on MSM SWIR albedo, class A having high albedo values >0.37 , class B having intermediate albedo values between 0.25 and 0.37 and class C with low albedo <0.25 . Figure 4 *b* shows occurrence frequency of these classes with respect to elevation from MOLA DEM. From Figure 4 *b* it is found that occurrence frequency of different classes shows some dependency on elevation. The spatial distribution of class B is remarkable in that it serves as a boundary between A and C. Each class occurs at all elevations between -4 to 6 km, where majority of the surface is represented. Class B and C are abundant below -4 km. At low elevations around -5 km, class C dominates the areal coverage. Class A seems to be evenly distributed over most elevations, and virtually absent at elevations less than -5 km. Figure 5 shows three classes of MSM-derived apparent albedo. Black colour represents no data values. Dark grey, grey and white coloured regions represent the MSM derived SWIR albedo values which are less than 0.25, 0.25 to 0.37 and more than 0.37 respectively.

Figure 6 shows the variation of weekly mean apparent albedo over three regions Syrtis Major, Daedalia Planum

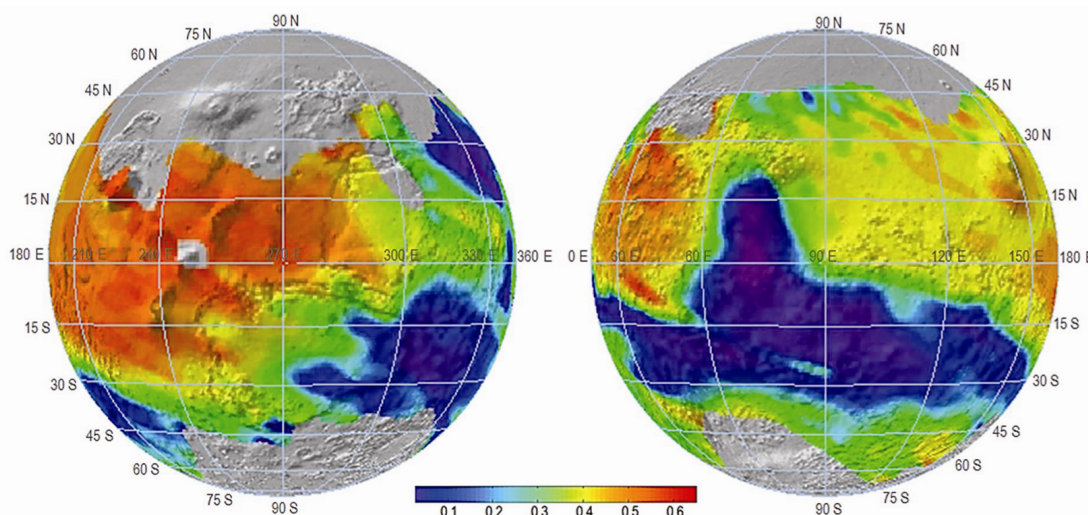


Figure 1. The 1 pixel per degree binned global MSM SWIR (1.65 μm) albedo map over MOLA map.

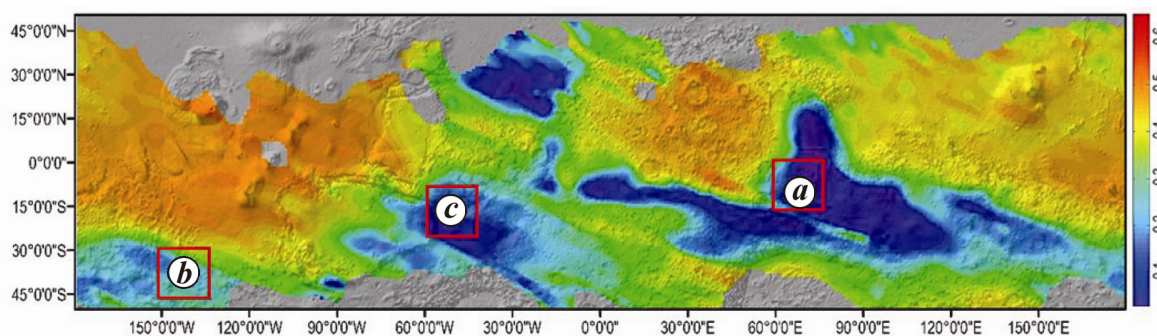


Figure 2. The MSM SWIR albedo map over MOLA background used for histogram analysis in Figure 3 and for comparison with OMEGA NIR albedo map. Latitude range is restricted to 50°. (a) Syrtis major region; (b) Daedalia Planum region; (c) Valles marineris region.

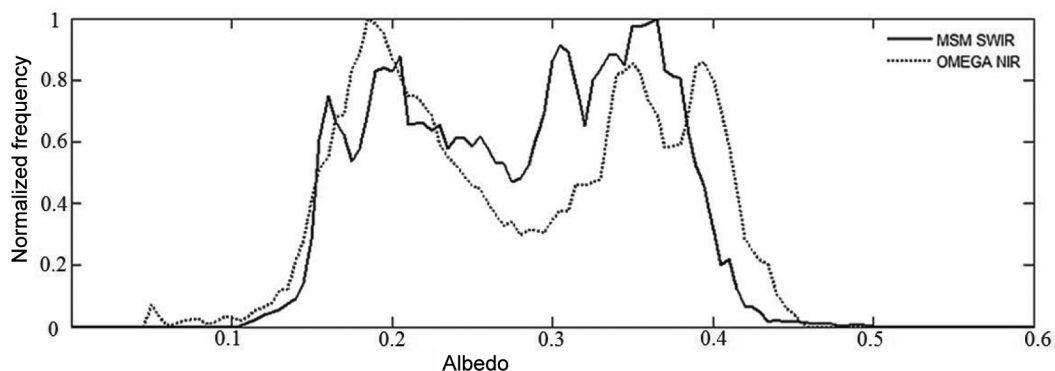


Figure 3. Normalized occurrence frequency of MSM SWIR and OMEGA NIR albedo.

and Valles Marineris region represented by red boxes in Figure 2. The following area is chosen to represent the low apparent albedo values. The data constraints are the same as in Figure 2. For each area the variation of apparent albedo with solar longitude, L_s is presented with data from each of the four months separated to allow a com-

parison of month-to-month variability. The bar represents the weekly variation of apparent albedo and the red point is the average value of weekly apparent albedo values. It was reported that the northern hemisphere during this period ($L_s = 205$ to 282) is known for dust activities, therefore the variations in apparent albedo shown in

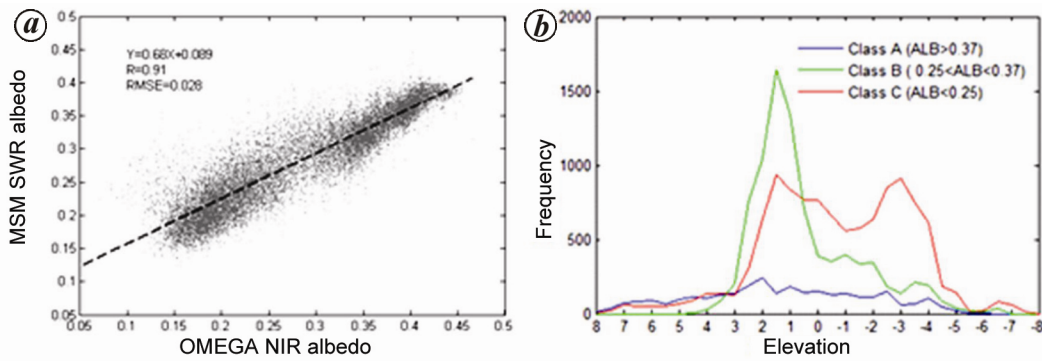


Figure 4. *a*, Scatter plot of MSM SWIR and OMEGA NIR albedo. *b*, Correlation of MOLA elevation with MSM SWIR albedo Classes. Different classes have clear elevation dependence here.

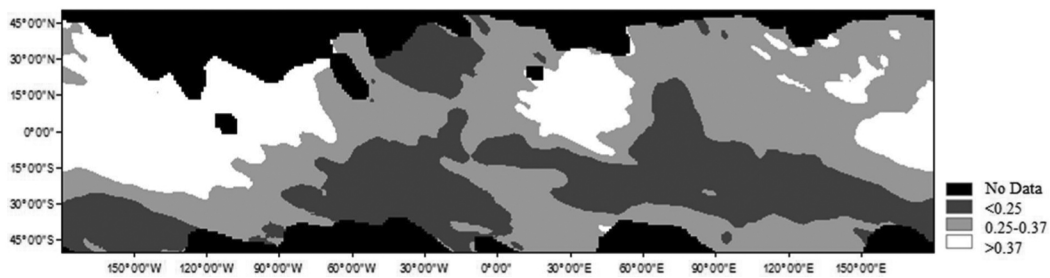


Figure 5. Three classes of MSM derived apparent albedo. Latitude range is restricted to 50°.

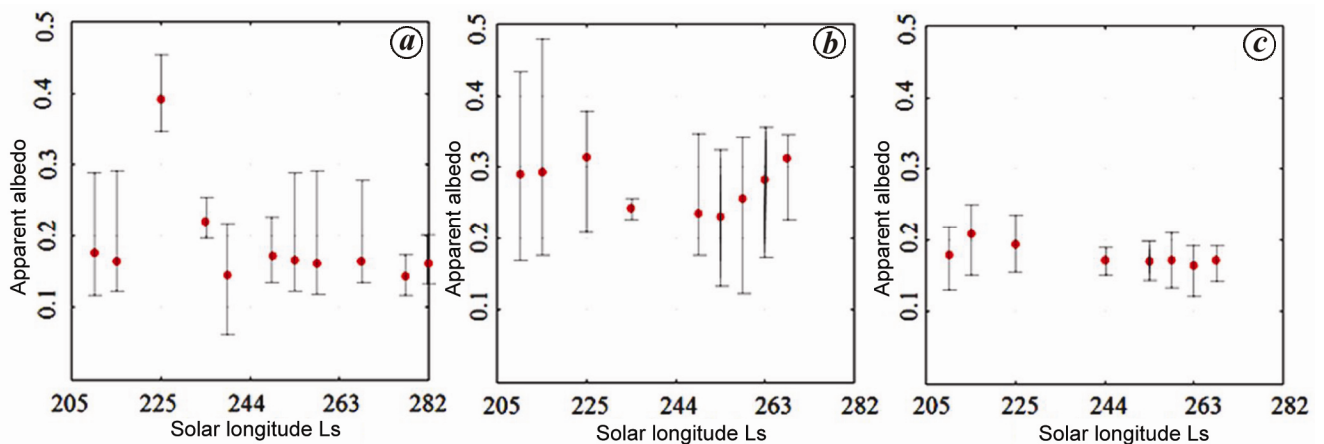


Figure 6. Variation of apparent albedo over (a) Syrtis Major Region (b) Daedalia Planum Region and (c) Valles Marineris Region. The data constraints are the same as given for Figure 2. The bar represents the weekly variation of apparent albedo and red point represents weekly mean apparent albedo.

Figure 6 may be related to the occurrence of local dust storms and transportation of atmospheric dust⁴. From Figure 6, it is clear that the variation of apparent albedo in Daedalia Planum and Valles Marineris falls within ± 0.1 about mean albedo, while Syrtis Major region shows pulsed increase of about 0.25 in albedo during October 2014. This high variation of apparent albedo in Syrtis Major was possibly due to local injection of dust into the atmosphere over Syrtis Major region which in turn increased the apparent albedo erratically around $L_s = 225$. It is to be noted that Christensen⁴, also showed similar behaviour of albedo variation in the Syrtis Major region.

Global apparent SWIR albedo map derived from MSM data acquired during the period of October 2014 to February 2015 is presented. Occurrence frequency of global apparent SWIR albedo shows a clear bimodal behaviour and is in good agreement with OMEGA NIR albedo distribution. The derived MSM apparent SWIR albedo are classified into three classes (high, intermediate and low albedo values), which show some elevation dependency. The derived MSM SWIR albedo over Syrtis Major, Daedalia Planum and Valles Marineris regions shows monthly variation with solar longitude, L_s which is directly linked with atmospheric dust activities.

1. De Vaucouleurs, G., *Physics of the Planet Mars*, Faber and Faber, London, 1952.
2. De Vaucouleurs, G., A low-resolution photometric map of Mars. *Icarus*, 1967, **7**, 310–349.
3. Kieffer, H. H., Martin, T. Z., Peterfreund, A. R., Jakosky, B. M., Miner, E. D. and Palluconi, F. D., Thermal and albedo mapping of Mars during the viking primary mission. *J. Geophys. Res.*, 1977, **82**, 4249–4292.
4. Christensen, P. R., Global albedo variations on Mars: implications for active aeolian transport, deposition and erosion. *J. Geophys. Res.*, 1988, **93**, 7611–7624.
5. Bibring, J.-P. *et al.*, ISM observations of Mars and Phobos: First results. Proceedings of the 20th Lunar Planetary Science Conference, 1990, pp. 461–471.
6. Mustard, J. E. *et al.*, The surface of Syrtis Major: composition of the volcanic substrate and mixing with altered dust and soil. *J. Geophys. Res.*, 1993, **98**, 3387–3400.
7. Soderblom, A., The composition and surface mineralogy of the Martian surface from spectroscopic observations: 0.3 μm to 50 μm , in Mars (eds Kieffer, H. H. *et al.*), Univ. of Ariz. Press, Tucson, 1992, pp. 557–593.
8. Bell, J. F. I. *et al.*, Near-infrared imaging of Mars from HST: surface reflectance, photometric properties, and implications for MOLA Data. *Icarus*, 1999, **138**, 25–35.
9. Mellon, M. T., Jakosky, B. M., Kieffer, H. H. and Christensen, P. R., High resolution thermal inertia mapping from the Mars global surveyor thermal emission spectrometer. *Icarus*, 2000, **148**, 437–455.
10. Smith, D. E. *et al.*, Mars Orbiter Laser Altimeter—Experiment summary after the first year of global mapping of Mars. *J. Geophys. Res.*, 2001, **106**(E10), 23689–23722.
11. Bibring, J.-P. *et al.*, OMEGA: Observatoire pour la Minéralogie, l'Eau, les Glaces et l'Activité, Eur. Space Agency Spec. Publ. *ESA SP*, 2004, **1240**, 37–49.
12. Sun, X., Neumann, G. A., Abshire, J. B. and Zuber, M. T., Mars 1064 nm spectral radiance measurements determined from the receiver noise response of the Mars Orbiter Laser Altimeter. *Appl. Opt.*, 2006, **45**(17), 3960–3971.
13. Heavens, N. G., The reflectivity of Mars at 1064 nm: derivation from Mars Orbiter Laser Altimeter Data and Application to Climatology and Meteorology. *Icarus*, 2016, **289**, 1–21.
14. Kiran Kumar, A. S. and Chauhan, P., Scientific exploration of Mars by first Indian interplanetary space probe: Mars orbiter mission. *Curr. Sci.*, 2014, **107**(7), 1096.
15. Ody, A. *et al.*, Global Maps of anhydrous minerals at the surface of Mars from OMEGA/Mex. *J. Geophys. Res. Planets*, 2012, **117**, 10.1029/2012JE004117.
16. Poulet, F. *et al.*, Martian surface mineralogy from Observatoire pour la Minéralogie, l'Eau, les Glaces et l'Activité on board the Mars express spacecraft (OMEGA/MEx): global mineral maps. *J. Geophys. Res.*, 2007, **112**, E08S02, 10.1029/2006JE002840.

ACKNOWLEDGEMENTS. We thank the support and encouragement provided by Shri Tapan Misra, Space Applications Centre (SAC), Ahmedabad, during this study. Support provided by Dr B. S. Gohil, Earth, Ocean, Atmosphere, Planetary Science and Applications Area (EPSA), SAC is thankfully acknowledged. We also thank the sensors and data products teams for providing the MSM data.

Received 29 February 2016; revised accepted 1 March 2017

doi: 10.18520/cs/v113/i01/112-116

Fracture behaviour of fibre reinforced geopolymer concrete

S. Sundar Kumar^{1,*}, K. C. Pazhani² and K. Ravisankar¹

¹CSIR-Structural Engineering Research Centre, Taramani, Chennai 600 113, India

²Anna University, Adyar, Chennai 600 025, India

Geopolymers have several applications and concrete is one of the materials that can be produced with geopolymer as binder. Since industrial byproducts/wastes such as fly ash, iron slag, micronized biomass silica, silica fume, red mud, etc. can be used as a binder instead of Portland cement, geopolymer concrete (GPC) has generated lot of interest among the scientific and engineering community. This has also resulted in reduced carbon footprint of concrete and an effective method of disposing industrial waste. In this study GPC with a blend of class-f fly ash and ground granulated blast furnace slag as binder has been developed, and its flexural and fracture characteristics have been studied. The GPC developed has a 28-day compressive strength in the range 40–50 MPa. Incorporation of steel fibres resulted in increased flexural strength, enhanced fracture properties and ductility. The residual strength of steel fibre reinforced GPC was also determined in the study.

Keywords: Alkali activators, fracture behaviour, fly ash, geopolymer concrete, iron slag, steel fibres.

CONCRETE is the second most consumed commodity by humans, and Portland cement (PC) has been the binder in concrete for centuries. However, there is also a parallel effort being made to reduce the consumption of cement. Being produced from naturally occurring calcareous and argillaceous materials, cement consumes a lot of energy and causes environmental degradation during excavation and processing of raw materials. In an effort to reduce cement consumption, industrial by-products such as iron slag and fly ash are being used as partial replacement for cement. Incorporation of fly ash and slag not only results in reducing the volume of cement used, but also leads to better quality of concrete. When these supplementary cementitious materials are incorporated in a proper manner, durability of concrete is enhanced without compromising on its strength. The use of slag in cement dates back to the 1940s, when attempts were made to activate slag using alkalis. The bibliographic history of important events in the development of alkali-activated cement has been documented by Li *et al.*¹. Alkali activation completely eliminates the use of PC, unlike partial replacement of cement with slag or fly ash. In 1979, Davidovits introduced the term 'geopolymer' and defined it as an

*For correspondence. (e-mail: ssk@serc.res.in)